Epidermal tumour-resistant progenitors require SOX2-driven developmental reprogramming to drive tumorigenesis

Patricia P. Centeno[1,2], Christopher Chester[2,4], Catriona A. Ford[1], Rachel A Ridgway[1], Patrizia Cammareri[1,5], Thomas Jamieson[1], Richard Marais[2,4], Andrew D. Campbell[1], Owen J. Sansom[1,3].

[1] Cancer Research UK Scotland Institute, Glasgow, UK.

[2]Cancer Research UK Manchester Institute, Manchester, UK.

[3]School of Cancer Sciences, University of Glasgow, UK.

[4]Present address: Oncodrug Ltd, Alderley Park, Macclesfield, UK.

[5]Present address: Cancer Research UK Scotland Centre, Institute of Genetics and Cancer, University of Edinburgh, Edinburgh, UK.

ABSTRACT

The epidermal basal layer consists of two distinct progenitor populations contributing differentially to skin homeostasis or wound healing. However, their resilience to oncogenic insults is unknown. Here, we developed mouse models allowing lineage tracing and oncogene expression in both populations. Our findings support the existence of two long-lived and functionally distinct epidermal progenitors and define them as tumour-primed and tumour-resistant. The tumour-primed progenitors drive cutaneous squamous cell carcinoma (cSCC), within days from oncogenic expression resembling the rapid onset of BRAF-inhibitor-driven cSCC. The tumour-resistant progenitors transform gradually, requiring SOX2 activation. Once transformed, they share a transcriptomic profile revealing molecular hallmarks of epidermal transformation independently of the cell-of-origin or the oncogenic driving mutations. Importantly, SOX2 is expressed in a subset of cSCC patients hinting at its cell-of-origin. These highlight the need for an in-depth understanding of the cell-specific vulnerabilities that apply in each tissue to open new avenues for rational treatment.

STATEMENT OF SIGNIFICANCE

Using *in vivo* models, we define tumour-primed and tumour-resistant epidermal progenitors and reveal SOX2-driven reprogramming as a driver of tumorigenesis in resistant cells. SOX2 expression in a subset of cSCC patients links to cell-of-origin, uncovering a cell-specific vulnerability that advances our understanding of cancer initiation and progression in epithelial tissues.

INTRODUCTION

Adult stem cells and progenitors continuously regenerate and maintain the mammalian epidermis, ensuring its structural integrity and protection against the external environment. However, the ageing skin accumulates a high mutational burden, including mutations in known drivers of cutaneous squamous cell carcinoma (cSCC) as well as passenger mutations [1]. The proliferation of these mutated cells is confined under normal conditions by the skin hierarchy and spatial compartmentalisation, but stressors such as wounding, inflammation, UV exposure, and certain oncogenic mutations can overcome these constraints leading to tumorigenesis [2–6]. cSCC originates from the keratinocytes, and data from murine model systems have illustrated the tumour's ability to form from different origins, including the hair follicle, the sebaceous glands, and the interfollicular epidermis compartments [2,7–9].

Two models have been proposed in the interfollicular epidermis to explain the basal layer heterogeneity. The first model described the existence of two distinct basal progenitors that contribute differently during homeostasis, wound healing [10] and mechanical stretching [6]. Upon wounding, these progenitors sense reduced cell density and enhance proliferation by undergoing symmetric self-renewing division, whilst the skin adopts a transient fluid-like state to facilitate progenitor migration

for regeneration and remodelling [11]. An alternative second model proposes that the heterogeneity of the basal layer is caused by different levels of commitment to differentiation, suggesting that a sole progenitor fuels epidermal maintenance [12]. Nevertheless, the comparison between these two distinct basal populations in response to oncogenic stimuli remains unexplored.

The most widely used cSCC mouse model is the well-established two-stage topical application of the chemical carcinogen 7,12-dimethylbenz[a]anthracene (DMBA), followed by the promoting agent 12-O-tetradecanoylphorbol-13-acetate (TPA) [2,13]. These tumours develop rapidly from the *Lgr6+* stem cells residing in the hair follicle and are predominantly driven by *Hras*^{Q61L} and *Trp53* mutations [2,14]. Nevertheless, mutations in *HRAS* are relatively uncommon in spontaneous human cSCC (9-16%) and found in healthy skin as passenger mutations [1,9,15]. However, HRAS-driven cSCC is commonly found in melanoma patients arising within weeks of treatment with BRAF^{V600E} inhibitors (BRAFi) [15–17]. This has been attributed to the paradoxical activation of the MAPK signalling pathway by BRAFi, due to the *HRAS*-mutations already present in the skin [17,18]. Spontaneous human cSCC exhibits high mutational burden, mutational heterogeneity and copy number alterations (Bailey et al., 2023), with the main driver mutations concentrated in the Notch (79.5%) and TP53 (71%) signalling pathways [3]. However, single mutations in these pathways are insufficient to induce cSCC in mice, and additional combinations of genetic driver alterations involving the TGFβ and MAPK signalling pathways, are required for transformation and modelling of disease progression [7,9,19,20]. The complexity and slow tumour progression of these models have hindered efforts in the field to understand the biology of skin carcinogenesis.

Here, we generated a suite of mouse models expressing different oncogenes targeted to two distinct basal populations of the interfollicular epidermis, marked by the expression of KRT14+/KRT5+ or IVL+, that rapidly model and resemble human cSCC. Particularly, we modelled the aetiology of fast-growing cSCC in melanoma patients driven by the hyperactivation of MAPK signalling after treatment with BRAFi. We defined a tumour-resistant and a tumour-primed population and uncovered a shared transcriptional programme involving the activation of embryonic, wound healing and tumour-specific keratinocyte signatures. Importantly, we identified SOX2 as a critical factor for the transformation of the tumour-resistant population. SOX2, highly expressed in ~25% of human cSCC, is known to induce stem cell characteristics as a super pioneer factor [21] and is recognised for its ability to reprogramme terminally differentiated somatic cells into induced pluripotent stem cells in concert with the so-called 'Yamanaka' stem cell factors. Our findings demonstrate the differential susceptibility of basal populations to transformation and reveal that tumours retain characteristics of their cells-of-origin, offering insights into patient stratification and highlighting specific cellular vulnerabilities during cSCC development.

RESULTS

Distinct basal populations coexist in the interfollicular epidermis and compete upon BRAF^{V600E} expression

To investigate the heterogeneity of the basal cells within the interfollicular epidermis, we first confirmed the presence of two distinct cell populations in the basal layer [10,12]. For this, we utilised the *Rosa26* LSL-tdTomato fluorescence protein (tdRFP) reporter transgene under the control of tamoxifen-inducible Cre recombinase expressed from two cell-specific promoters: the *Krt14* promoter (*Krt14*-CreERT2; hereafter K14) to target the basal stem-like population, and the *Ivl* promoter (Ivl-CreERT; hereafter Ivl) to target the suprabasal layer and the basal committed population (**Fig. 1A**). Lineage-tracing experiments were conducted on day 8 and day 28 post tdRFP induction, three times roughly the vertical epidermis turnover time in mice (**Fig. 1B**). In the K14:tdRFP model, all cells in the basal layer and their progeny in the suprabasal layers were labelled at day 8, and both epidermal layers remained labelled at day 28 (**Fig. 1C and D**). In the Ivl:tdRFP model, the labelled cells were mainly located in the suprabasal layer with a few labelled cells in the basal layer at day 8 (**Fig. 1C and E**). By day 28, the basal IVL/RFP+ labelled cells had now divided forming small stable clones contributing with their progeny to the suprabasal layer (**Fig. 1C and F**). Nevertheless, suprabasal cells that were not located under a label retainer IVL+ basal cluster turned over and those regions lost any tdRFP label.

We confirmed IVL expression in the basal layer of the mouse interfollicular epidermis by immunohistochemistry (**Fig. 1G**). Moreover, the tdRFP label was retained for up to 180 days post-induction marking a long-residing stable population of the basal layer (**Fig. 1H**). We also confirmed KRT14 and KRT5 (basal markers) ubiquitous expression in all cells within the basal layer by immunohistochemistry (**Supplementary Fig. S1A**).

To gain further insights into the tumorigenic capacity of these distinct pools of progenitors, we used the potent oncogene BRAF$^{V600E/+}$ which hyperactivates the pro-proliferative MAPK signalling pathway. MAPK hyperactivation drives rapid cSCC in melanoma patients treated with BRAFi [15–17]. Moreover, oncogenes in this pathway, such as KRAS^{G12V} and HRAS^{G12D}, have been used to drive cSCC in mouse models in combination with other drivers [7,9,19].

We generated a suite of mouse models in which we could induce and follow BRAF^{V600E} expressing populations under its endogenous promoter once tamoxifen activates Cre recombinase in IVL+ or KRT14+ expressing cells. This in turn induces the coexpression of tdRFP reporter that provides and approximation of mutated cells (Ivl:BRAF^{V600E}-tdRFP and K14:BRAF^{V600E}-tdRFP). We conducted lineage-tracing analysis in both models, on day 8 post BRAF^{V600E} oncogene and tdRFP induction, before any

macroscopic changes appeared in the skin. As expected in the K14: BRAF^{V600E}-tdRFP model, all cells in the basal layer and their progeny in the suprabasal layer were labelled. The only difference with the K14:tdRFP model was the marked increase in proliferation shown by Ki67 staining (**Fig. 1D**).

Upon oncogene activation in the Ivl:BRAF^{V600E} -tdRFP model, we observed a vast increase in the number of labelled basal cells which overtook the unlabelled population. This was in line with the increase in the number of cells expressing the proliferation marker Ki67 (**Fig. 1E)**. In sharp contrast, in the Ivl:tdRFP model the IVL+ labelled population was a minority. Thus, IVL and K14 mark distinct progenitor cell types that coexist in the basal layer and that both can give rise to differentiated progeny that migrate to suprabasal layers and are susceptible to oncogene-induced proliferation.

Tumour-primed and tumour-resistant populations coexist in the basal layer

To study the susceptibility of the two different basal populations to transformation and tumour formation upon BRAF^{V600E} oncogene activation, we used the K14 and *Krt5* promoter (K5-CreERT; hereafter K5) and the *Ivl* promoter to drive oncogene activation at our targeted populations (**Fig. 2A**). Upon BRAF^{V600E} oncogene induction, both K14+ and K5+ cells rapidly formed tumours (8 days to tumour onset), suggesting that they are permissive to tumour development and primed for oncogenic transformation. This contrasted with the tumour-resistant IVL+ cells, which required a much longer time to develop tumours (125 days to tumour onset) (**Fig. 2B-2D**).

We also observed that the Ivl:BRAF^{V600E} model tends to develop multiple tumours at different body sites, including the back, paws, ears and lips. In contrast, the K5- and K14-driven BRAF^{V600E} models mainly develop one tumour on their back at the precise area of tamoxifen application (**Fig. 2E**). Moreover, reducing the dose and duration of the tamoxifen-induction regimen in the K5:BRAF^{V600E} and K14:BRAF^{V600E} models delayed tumour onset, but tumours still grew at a fast rate (**Fig. 2F**). The longer latency period for tumours to develop in the Ivl:BRAF^{V600E} model suggests that the IVL+ population requires additional cooperating events to facilitate tumour onset. Thus, we exposed the back of the Ivl:BRAF^{V600E} mice to mild UV [four weekly doses 6 standard erythema doses (SED)], but it did not accelerate tumour onset despite UV being a risk factor for cSCC due to its increase in mutation burden (**Fig. 2B**). Similarly, topical treatment with the inflammation-promoting agent known to stimulate epidermal proliferation, TPA, (three times per week) did not accelerate tumorigenesis either (**Supplementary Fig. S1B**). Lineage-tracing experiments, conducted in the Ivl:tdRFP model in the presence and absence of TPA, on day 28 post-induction showed neither increased proliferation nor IVL+ clonal expansion (**Supplementary Fig. S1C**).

Transplantation of subcutaneous pieces from K5:BRAF^{V600E}-derived tumours into C57BL/6J and NSG-II2 immunodeficient mice revealed cancer stem cell potential and a rapid ability to form secondary

145 tumours **(Fig. 2G)**. No statistical differences in tumour onset were seen between K14:BRAF^{V600E} cohorts
146 housed in two different establishments or by sex (**Fig. S1D and S1E**). However, the Ivl: BRAF^{V600E} model
147 showed a shorter tumour onset in the cohort housed at the CRUK SI while no differences were seen
148 between sexes (**Supplementary Fig. S1F and S1G**).

149 Overall, despite both populations residing in the basal layer and sharing the microenvironment, they
150 show profound differences in susceptibility to transformation upon BRAF^{V600E} oncogene induction.

151 Shared transcriptional landscape of different epidermal populations upon 152 transformation

153 We characterised the histopathological features of tumours originating in the K5:BRAF^{V600E},
154 K14:BRAF^{V600E}and Ivl:BRAF^{V600E} models and found remarkable similarities. All tumours were formed by
155 vertical columns of keratinocytes with clearly demarcated limits (**Supplementary Fig. S2A**). Detailed
156 immunohistochemistry showed distinctive pathological features of cSCC. These included enlarged
157 interfollicular epidermis and cornified layers with aberrant accumulation of extracellular keratin
158 (keratin pearls), nuclear atypia, and incomplete maturation of keratinocytes (parakeratosis) as the
159 keratinocytes in the cornified layer retain their nuclei (**Fig. 2H and Supplementary Fig S2B**).

160 The tumours presented the hallmarks of papilloma with signs of squamous differentiation, as
161 demonstrated by the increase in the number of layers, expressing the basal markers KRT5 and KRT14,
162 but also the suprabasal marker KRT1 (**Fig. 2I and Supplementary Fig. S2C**). In the most advanced cases,
163 these markers were expressed throughout the entire epidermal layer indicating a complete loss of
164 cellular hierarchy and disruption of multi-layer organisation. Moreover, the increase in Ki67 denotes
165 epidermal hyperproliferation and hyperplasia of the interfollicular epidermis. These lesions were
166 highly proliferative, recapitulating the rapid onset and histopathology observed in human cSCC (**Fig. 2J
167 and Supplementary Fig. S2D**).

168 Given the similarities in histology, we next assessed whether transcriptional profiling could identify
169 potential long-lasting markers of the cell-of-origin of these tumours. Firstly, we performed a batch
170 correction to correct for any bias arising from batches sequenced at different times (**Supplementary
171 Fig. S3A**). Then, we examined potential differences between the K5:BRAF^{V600E} and K14:BRAF^{V600E}
172 models, as the respective tumours arose from the same cell populations simultaneously expressing
173 both KRT5 and KRT14. They clustered independently of the model, and our analysis returned no
174 differentially expressed genes, so we merged these samples for further transcriptomic analysis
175 (**Supplementary Fig. S3B and S3C**). Thus, we compared K14/K5:BRAF^{V600E}- and Ivl:BRAF^{V600E}-derived
176 tumours against normal skin from control littermates. Unsupervised clustering and principal
177 component analysis (PCA) showed that the tumours separated from the normal skin samples (**Fig. 3A**

178 **and B**). Interestingly, the vast majority of upregulated genes (82.8%) were shared between the
179 K14/K5:BRAF^{V600E} and Ivl:BRAF^{V600E} tumours (**Fig. 3C and D**).

180 Gene set enrichment analysis of differentially expressed genes highlighted commonly upregulated
181 signatures including those associated with the *Myc*, *Lgr5* and *Lgr6* wound healing response [22],
182 embryonic epidermis [23], and the human-derived tumour-specific keratinocyte population [24] among
183 others (**Fig. 3E and Supplementary Fig. S3D**). Next, we examined the expression of selected
184 differentially expressed genes across samples. We observed high expression of *Myc*, the known cSCC
185 markers *Krt6a* and *Krt6b* [25], and *Anxa1* ligand, which is secreted by wounded epithelia during
186 regeneration and re-epithelisation [22] (**Fig. 3F**). ANXA1 is also enriched in the tumour-specific
187 keratinocyte population signature [24], and it has been shown to play a tumour-promoting role in other
188 cancers of epithelial origin such as cancers of the prostate [26] and breast [27]. We also found increased
189 expression of the basal marker *Ly6a* [22] which, together with *Anxa1*, have been proposed as a marker
190 of foetal reprogramming and regenerative stem cells in the regenerating colonic epithelium and
191 colorectal tumours (Gil Vazquez et al., 2022; Yui et al., 2018).

192 In addition, we found upregulation of *Myc,* which has been identified in wound healing as a crucial
193 transcription factor during sebaceous duct dedifferentiation generating a broad range of interfollicular
194 epidermis cells that contribute to re-epithelialisation [5]. We also observed increased expression of the
195 interleukins *Il24* and *Il6*. Interestingly, a recent model for tissue injury-sensing uncovered the role of
196 IL24, produced at wound sites in response to hypoxia, in promoting epithelial proliferation and re-
197 epithelialisation via pSTAT3 activation [30]. This pathway may also extend to cSCC, as we see increased
198 expression of the hypoxia sensor HIF1α and IL24, and pSTAT3 in our models (**Fig. 3F and G**). In addition,
199 IL6 stimulates the release of proinflammatory cytokines from the cutaneous microenvironment in
200 response to wounding, activating TGFβ receptor signalling and the STAT3 signal transduction pathway
201 [30,31].

202 These transcriptomic results were validated by RNAscope for *Ly6a*, and immunohistochemistry for
203 MYC, ANXA1 and pSTAT3 in our K14:BRAF^{V600E} and Ivl:BRAF^{V600E} models (**Fig. 3G**). Similar findings were
204 seen in tumours originating from the hair follicle stem cells upon MAPK signalling hyperactivation and
205 deletion of the TGFβ receptor 1 (*Alk5*) (Lgr5:BRAF^{V600E}-ALK5$^{fl/fl}$, Lgr5:HRAS$^{G12V/G12V}$-ALK5$^{fl/fl}$,
206 Lgr5:KRAS$^{G12D/+}$-ALK5$^{fl/fl}$) [9] and deletion of *Trp53* and *Notch2* (Lgr5:TRP53$^{fl/fl}$-NOTCH2$^{fl/fl}$)
207 (**Supplementary Fig. S3E**).

208 Overall, these results reveal shared molecular and transcriptional hallmarks of epidermal
209 transformation independently of the cell-of-origin, tumour latency, or the oncogenic driver mutations.

The tumour-resistant basal population depends on SOX2 for transformation

To further investigate the tumours arising from the two distinct basal cell populations, we grouped tumours from K5/K14:BRAF^{V600E} and Ivl:BRAF^{V600E} models and compared their transcriptomic profiles revealing only a handful of differentially expressed genes (**Fig. 4A**). Notably, SOX2 emerged as a key transcriptional difference, being highly and selectively enriched in Ivl:BRAF^{V600E} tumours, relative to K5/K14:BRAF^{V600E} (**Fig. 4A**).

SOX2 has been identified as a super pioneer transcription factor able to bind to close chromatin through its ability to interfere with the maintenance of DNA methylation [21]. Furthermore, SOX2 is commonly used as a marker of cancer stem cells and is upregulated in cSCC patients, where it appears to rewire cells for tumour initiation and growth [32,33]. We confirmed SOX2 expression by immunohistochemistry in Ivl:BRAF^{V600E} tumours (**Fig. 4B**). Meanwhile, SOX2 expression was negligible in normal skin during homeostasis (**Supplementary Fig. S4A**), and in tumours of K5:BRAF^{V600E} or K14:BRAF^{V600E} origin (**Fig. 4B**). We also assessed SOX2 levels in TPA-treated skin and detected no immunoreactivity suggesting that its expression is not linked to inflammation **(Supplementary Fig. S4B)**. We then extended our investigation to a broader suite of models. We found SOX2 expressed in DMBA/TPA-induced tumours (**Supplementary Fig. S4C**) but not in tumours originating from *Lgr5+* cells (hair follicle bulge) driven by different oncogene combinations (**Supplementary Fig. S4D**).

To highlight the cell-specific role of SOX2, we assessed the expression of SOX9, a different master regulator of chromatin accessibility that switches embryonic epidermal cells to a hair follicle stem cell fate and is also constitutively active during tumorigenesis [34]. As reported, we found that SOX9 was expressed mainly in the hair follicle cells in healthy skin homeostasis, and its expression was increased in the basal layer of all the tumours irrespective of the cell of origin (**Supplementary Fig. S4E**). Therefore, the transcriptional output of BRAF^{V600E} activation is dependent on the cell-specific context. The suprabasal markers KRT4 and KRT13, commonly expressed in skin homeostasis, were also differentially expressed between the K5/K14:BRAF^{V600E} and Ivl:BRAF^{V600E} models (**Fig. 4A**). However, mRNA expression levels did not correlate with increased protein levels as we found no significant differences in immunostaining intensity across our models (**Supplementary Fig. S4F**).

Given the potential aetiological activation of SOX2 in skin tumorigenesis, we crossed the K14:BRAF^{V600E} and Ivl:BRAF^{V600E} models with mice harbouring a conditional *Sox2* knockout allele (SOX2^{fl}) (**Fig. 4C**). While conditional *Sox2* deletion did not affect tumorigenesis or tumour growth in the K14:BRAF^{V600E}-SOX2$^{fl/fl}$ model (**Fig. 4D**), it significantly delayed tumour onset and tumour growth in the Ivl:BRAF^{V600E}-SOX2$^{fl/fl}$ model (**Fig. 4E**). Loss of *Sox2* had no impact on skin homeostasis, consistent with its lack of expression in normal skin. The histopathological features of K14:BRAF^{V600E}-SOX2$^{fl/fl}$ and Ivl:BRAF^{V600E}-

243 SOX2$^{fl/fl}$ tumours were similar to those expressing the wild-type *Sox2* allele, including an enlarged
244 epidermis displaying vertical columns of keratinocytes, incomplete maturation of keratinocytes,
245 increased proliferation indicated by Ki67 immunoreactivity mainly in the basal layer, and MYC and
246 pSTAT3 activation (**Fig. 4F and Supplementary Fig. S5**). Interestingly, certain patches within
247 Ivl:BRAF^{V600E-} SOX2$^{fl/fl}$ tumours show recombination escaping clones that retained SOX2 expression,
248 indicating that its expression contributed to tumorigenesis (**Fig. 4G**). However, such SOX2+ escapee
249 patches were not observed in the K14:BRAF^{V600E-}SOX2$^{fl/fl}$ tumours (**Supplementary Fig. S5**).

250 To confirm the role of SOX2 in the tumour-resistant population, we crossed the Ivl:BRAF^{V600E} model
251 with an allele overexpressing SOX2 after tamoxifen induction *Rosa26*LSL-SOX2-IRES-eGFP (hereafter
252 SOX2^{LSL}). The overexpression of SOX2 in combination with BRAF^{V600E} in this population significantly
253 accelerated tumour onset to 34.5 days, while SOX2 overexpression on its own showed no phenotype
254 (**Fig. 4E**).

255 Overall, these results highlight SOX2 activation as a specific requirement for the IVL+ population to
256 drive tumorigenesis.

257 Expression of SOX2 hints at a cell-of-origin for cSCC patients and drives developmental
258 and juvenile epidermal signatures.

259 Around 25% of cSCC from human patients show high or medium expression levels of SOX2 [33,35]. We
260 further validated this finding in a human dataset [19]containing transcriptional data from different stages
261 of disease progression. We observed that *SOX2* levels were increased in 27% of premalignant actinic
262 keratosis (AK) and 35% of cSCC lesions, whereas *SOX2* expression levels were low in normal skin (NS)
263 (**Fig. 5A**). These results underscore a diverse cell origin for cSCC. Besides, they align with the hypothesis
264 that SOX2 is only required for the transformation of a particular IVL+ basal population, whereas it is
265 not required for the transformation of K5/K14+ basal population or metastatic competence.

266 To further explore the role of SOX2 activation in human keratinocytes, we first immortalised two
267 healthy human epidermal keratinocyte cell lines, derived from a juvenile and an adult donor, by
268 introducing hTERT overexpression and p16 knockout. We subsequently overexpressed SOX2 in the
269 derivative cell lines (**Fig. 5B and C**) and investigated their transcriptomic profiles by bulk RNAseq. SOX2
270 overexpression triggers transcriptomic changes in the adult cell line, separating it from the parental
271 cell line, while only small transcriptomic changes were seen in the juvenile SOX2-expressing cell line
272 that cluster with its parental line (**Fig. 5D**). The profound SOX2-driven changes in the adult
273 transcriptome included significant enrichment for the embryonic and juvenile epidermal signatures
274 even without additional oncogenes (**Fig. 5E-G**). Interestingly, this enrichment was not observed in the
275 SOX2 overexpressing juvenile cell line (**Supplementary Fig. S6A-S6C**). This could be due to the juvenile

276 cell line already expressing an embryonic/juvenile-like transcriptome, hence SOX2 cannot drive further
277 changes. Nevertheless, it enriched for MYC hallmarks required for tumour growth (**Supplementary Fig.**
278 **S6B and S6C**), as we have seen in our murine models independently of the cell of origin (**Fig. 3E and**
279 **G**).

280 Dabrafenib as a tumour-promoter in *HRAS*-mutated epidermis

281 Patients of cSCC often carry mutations in the *HRAS* gene causing hyperactivation of MAPK signalling.
282 Thus, we tested whether we could drive tumours from distinct basal cell populations using an *Hras*^{G12V}
283 allele, which encodes a different upstream oncogenic effector of the MAPK signalling pathway. We
284 expressed the *Hras*^{G12V} allele in the K14+ and IVL+ cell populations under its endogenous promoter
285 (**Fig. 6A**). Nevertheless, this oncogene was not as potent at driving transformation as *Braf*^{V600E}.
286 Expression of one copy of the *Hras*^{G12V} allele in the K14+ population did not result in tumorigenesis
287 (**Fig. 6B**). Two copies of this allele resulted in mice becoming unwell, probably due to the critical
288 function of HRAS in the gastrointestinal epithelium before any skin-related malignancies appeared.
289 Nevertheless, K14:HRAS$^{G12V/G12V}$ mice showed hyperproliferation of the skin basal layer, evidenced by
290 increased Ki67 expression, mild MYC activation, and strong pSTAT3 activation at the time of sampling
291 (**Supplementary Fig. S7**). In the IVL+ basal population, one copy of the HRAS^{G12V} allele was not
292 sufficient to drive tumorigenesis, but two copies of the allele drove tumorigenesis with a tumour-free
293 survival of 24 days (**Fig. 6C**). The resulting tumours displayed similar hallmarks to Ivl:BRAF^{V600E} tumours
294 including vertical columns of immature keratinocytes, increased expression of the proliferation marker
295 Ki67, MYC and pSTAT3 activation, and patches of SOX2 activation (**Supplementary Fig. S7**).

296 Interestingly, melanoma patients commonly treated with BRAFi , such as Dabrafenib, have an increased
297 risk of developing cSCC due to the presence of dormant *HRAS* mutations in the skin (Hauschild et al.,
298 2012; Oberholzer et al., 2012; Su et al., 2012). Consequently, these patients develop fast-growing
299 tumours within weeks of treatment, driven by the paradoxical activation of the MAPK signalling
300 pathway. This rapid cSCC development resembles what we have seen in our K5:BRAF^{V600E} and
301 K14:BRAF^{V600E} models. Thus, we treated Ivl:HRAS$^{G12V/+}$ and K14:HRAS$^{G12V/+}$ mice with Dabrafenib three
302 times a week to mimic the patient dosing regimen and promote tumorigenesis. Indeed, this resulted
303 in tumorigenesis with a tumour-free survival rate of 22 days for the K14:HRAS$^{G12V/+}$ model and 58 days
304 for the Ivl:HRAS$^{G12V/+}$ model (**Fig. 6B and C**). These results align with the K14 population being tumour-
305 primed and IVL being tumour-resistant. Dabrafenib-promoted tumours exhibited keratin pearls,
306 parakeratosis, and nuclear dysplasia, together with increased expression of MYC, Ki67, pSTAT3
307 activation and, in the case of Ivl:HRAS$^{G12V/+}$ tumours, SOX2 activation (**Fig. 6D**). These models mimic the
308 rapid onset of cSCC seen in patients receiving BRAFi therapies and highlight its risk. Moreover, we also
309 treated with Dabrafenib healthy-looking mice carrying HRAS^{G12V} in the K14+ and IVL+ mutations at

310 180±5 days post-oncogene induction. These aged treated mice rapidly developed tumours within 25
311 days from the Dabrafenib treatment start, at similar latency in both models, mimicking the onset of
312 cSCC from melanoma patients carrying *HRAS* mutations (**Fig. 6E**).

313 DISCUSSION

314 The interfollicular epidermis basal layer is formed by two distinct populations that relate to different
315 levels of commitment to differentiation. There is still considerable debate whether these represent
316 two distinct progenitor populations or whether there is a single progenitor and its progeny. Here, we
317 show that the basal IVL+ is a long-lived minority population able to proliferate, generate small clones,
318 and differentiate. Therefore, our results support the existence of two long-lived and functionally
319 distinct epidermal progenitors [6,10,11] and contrast with the single progenitor model that classifies the
320 IVL+ population as a post-mitotic differentiating cell with a short residence in the basal layer [12].

321 One key question was whether these distinct basal populations had the same tumour-initiating
322 capacity following oncogenic mutations. Although both progenitors could contribute to epidermal
323 turnover and maintenance they had different permissiveness to tumorigenesis. MAPK signalling
324 hyperactivation through $BRAF^{V600E}$ expression in the basal K14+/K5+ population drove rapid
325 tumorigenesis with tumours developing within days of oncogene induction; hence, we called this
326 population tumour-primed. $BRAF^{V600E}$ expression in the IVL+ population bestowed a competitive
327 advantage over IVL- wild-type cells in the basal layer such that mutated cells expanded over the entire
328 basal epithelium just a week after oncogene expression. However, Ivl:$BRAF^{V600E}$ cells did not rapidly
329 develop into tumours and remained within an otherwise normal-looking epithelium. Thus, we termed
330 this latter population tumour-resistant. At longer latency, these cells progressed to tumorigenesis, and
331 tumours resembled those originating from K5+/K14+ cells. Expression of $HRAS^{G12V}$ or $KRAS^{G12D}$
332 oncogenes in the skin epithelium also outcompeted the wild-type population in homeostasis [36]. The
333 competitive advantage of oncogene-expressing cells that look histologically normal has also been seen
334 in blood cells and intestinal epithelium [37,38].

335 The differential permissiveness to oncogenic transformation of IVL+ and K5+/K14+ populations aligns
336 with the behaviour observed during mechanical stretching and wound healing. In these situations, the
337 K5+/K14+ population are the first and main responders to epithelium repair and regeneration. The
338 K5+/K14+ population can swiftly bias its cell division towards a symmetric division promoting
339 proliferation to generate mass, while IVL+ cells make only a small contribution [6,10,11]. Similarly, in the
340 oesophagus epithelium, carcinogenesis is caused by a progenitor biasing cell division towards
341 symmetric proliferation [39]. The limited capacity of the IVL+ basal population to switch to symmetric

342 division and its tendency to preferentially undergo asymmetric division is part of its transcriptome-
343 engrained commitment towards differentiation and could explain its tumour-resistant phenotype.

344 Tumours arising from an IVL+ or a K5+/K14+ origin share a common transcriptional landscape that is
345 enriched for an activated wound-healing response [22], embryonic developmental pathways [23] and a
346 tumour-specific keratinocyte population seen in human cSCC [24]. In addition, we observed strong MYC
347 activation across all tumours, which has been proposed as a mechanism to confer stem cell properties
348 and dedifferentiation in the *Gata6*+ epidermal populations [5]. At the same time, we revealed evidence
349 of hijacking the tissue injury-sensing and repair pathway, triggered by hypoxia, and driven by IL24 and
350 STAT3 activation that resolves in a coordinated tissue repair after wounding [30]. Similar to wounds, the
351 core of a tumour is hypoxic, and we observed increased transcription of *Hif1a* and *Il24*, as well as STAT3
352 phosphorylation that enhanced oncogene-driven proliferation to generate the critical tumour mass
353 required for progression. These results highlight the close interplay between proliferation during
354 tumorigenesis, and re-epithelisation during wound sealing. Both processes involve the blood vessels,
355 fibroblast, and extracellular matrix remodelling.

356 One of our key findings was that the tumour-resistant population depends on SOX2 activation for
357 transformation; knocking out this gene delayed tumour onset and growth but did not affect the
358 tumour-primed population. Importantly, SOX2 overexpression within the Ivl:BRAF^{V600E} population
359 rapidly accelerated tumorigenesis showing that SOX2 is both necessary and sufficient for
360 transformation of the IVL+ lineage. Tumours generated using the DMBA/TPA protocol, also expressed
361 SOX2 suggesting a common origin. SOX2 is a super pioneer factor able to bind closed chromatin and
362 rewire the epigenome to drive stem cell features [21,40]. SOX2 expression has been reported in cSCC
363 patients and its activity confers tumour-initiating potency and stem cell traits [32,33]. Furthermore,
364 around 25% of cSCC patients express high levels of SOX2[33,35], suggesting that the IVL+ basal population
365 may act as a cell-of-origin for these tumours. Notably, previous studies examining tumorigenesis from
366 different cell types of the intestinal epithelium (progenitors from the crypt versus terminal differentiate
367 villus cells) were unable to find molecular changes associated with tumorigenesis coming from these
368 different cell types[41]. This contrasts with our findings here where SOX2 both marks and is functionally
369 required for the tumours arising from the IVL+ population but not for the K5/K14+ populations.

370 SOX2 overexpression in an adult human keratinocyte cell line increased the expression of
371 transcriptional signatures reflective of embryonic and juvenile epidermal cells implying that it can
372 rewire the epigenome to drive dedifferentiation and allow transformation. This is consistent with a
373 proposed bi-stable transcriptional network governed by PITX1 that precedes SOX2 and TRP63
374 expression and promotes cell proliferation and inhibition of differentiation by acting on KLF4 [42]. This

375 network would allow the tumour to switch between two states; proliferation and self-renewal or
376 differentiation and keratin pearl formation. We hypothesize that upon oncogene expression the IVL+
377 tumour-resistant population depends heavily on the activation of SOX2 axis to suppress, freeze, or
378 completely abolish its commitment towards differentiation by re-expressing basal makers. IVL+ cells
379 may dedifferentiate and become IVL- to drive tumorigenesis and to remain in the basal layer, where
380 the proliferative environment is confined.

381 These results are similar to studies within the oesophageal epithelium, where SOX2 is expressed in
382 adult progenitors during homeostasis and becomes overexpressed in oesophageal squamous cell
383 carcinoma. Once overexpressed, SOX2 drives a different transcriptional program by changing its
384 partner to KLF5, which drives STAT3 activation and tumorigenesis [43,44]. Thus, activation of SOX2 in the
385 cancer context would not necessarily signal through its traditional partners, *Pou5f1 (Oct4) and Nanog*,
386 that lead to pluripotent embryonic stem cells, but through a tissue or even cell-specific signalling
387 network that allows escaping any proliferation constraints with some hints from its embryonic
388 development. SOX2 is also expressed in a stem-cell enriched population in aggressive head and neck
389 cancer where it appears linked to smoking and HPV-positive patients [45]. How SOX2 is activated by
390 oncogenic mutations is still elusive. It may be directly or indirectly downstream of the commonly
391 activated pERK or MYC signalling pathways.

392 Our murine models resemble the rapid cSCC development, seen in melanoma patients treated with
393 BRAFi, due to paradoxical MAPK signalling activation [15–17]. Thus, we further modelled the cSCC
394 aetiology in these patients by mimicking patient treatment with the commonly used in-clinic BRAFi,
395 Dabrafenib. We found that Dabrafenib promoted the development of tumours from cells carrying
396 $HRAS^{G12V}$ mutations that had been sitting in the skin for up to 180 days without driving transformation.
397 It is important to note that in human tumorigenesis HRAS mutations in cSCC are relatively rare but
398 very common in patients that have developed cSCC following BRAF inhibitors. These also occur at rapid
399 latency, showing that the skin can tolerate mutations in oncogenic pathways with little histological
400 change and can rapidly progress to tumorigenesis given a specific stimulus or promoter.

401 Collectively, we have generated new *in vivo* models to study cSCC and characterised the response of
402 two distinct basal populations in the skin epithelium to oncogenic insults. We have defined a tumour-
403 primed and a tumour-resistant population able to drive cSCC. Importantly, SOX2 emerged as a critical
404 epigenetic regulator required to drive tumour growth from the IVL+ tumour-resistant population,
405 which also serves as a marker for identifying and classifying human cSCC according to the cell-of-origin.
406 Further characterisation of the different cSCC cells-of-origin and their vulnerabilities to transformation
407 will allow the development of rational cancer therapies to contain tumours at their source. For

408 example, by manipulating the cell-division bias towards differentiation rather than proliferation and
409 self-renewal. Nevertheless, this will require a deep understanding not only of the tissue-specific
410 mechanisms that drive transformation but also of the cell-specific vulnerabilities that govern epithelial
411 maintenance in homeostasis and tumorigenesis.

412 MATERIAL AND METHODS

413 Genetically engineered mouse models and husbandry

414 Mice were housed in accordance with UK Home Office Regulations, maintained in a pathogen-free
415 facility under a 12-h light-dark cycle at a constant temperature between 19–23°C, and 55 ± 10%
416 humidity, and given drinking water and fed standard chow diet *ad libitum*. Experiments conducted at
417 the CRUK Scotland Institute Animal Facility were in accordance with the UK Home Office guidelines,
418 under project licence PP3908577, and were reviewed and approved by the University of Glasgow
419 Animal Welfare and Ethical Review Board (AWERB). Experiments conducted at the CRUK Manchester
420 Institute were performed at Alderley Park Animal Research Unit, with breeding at the University of
421 Manchester incubator breeding facility, in accordance with UK Home Office regulations, under project
422 licences PE4369EDB and P671A5B06, and reviewed and approved by the CRUK Manchester Institute's
423 AWERB. Animals were monitored regularly until terminally sacrificed by schedule 1 at clinical endpoint:
424 either when the cumulative tumour burden had reached a maximum volume of 1500 mm^3 or when a
425 single tumour exceeded 15 mm in diameter, weight loss >20%, or any other signs of ill health and
426 distress. For all mouse studies, no formal randomisation was performed, and researchers were not
427 blinded to the mouse genotypes. No exclusions were performed and all mice included in experimental
428 cohorts were included in the analysis.

429 Genotyping was performed by Transnetyx according to the previously published protocols provided in
430 the references for each allele. Mice were maintained on a C57BL/6J background, carrying the following
431 alleles/transgenes: *Ivl*-CreERT2 [7], *Krt5*-CreERT2 [46], *Krt14*-CreERT2 [47], $BRAF^{V600E}$ [48,49], $HRAS^{G12V}$ [50],
432 *Rosa26LSL-tdRFP* [51], $Sox2^{fl}$ [52] and *Rosa26LSL-SOX2-IRES-eGFP* [53]. Archived tumour blocks [from[9]]
433 included the additional following alleles: *Lgr5*-CreERT2 [54], $Kras^{G12D}$ [55], $Notch2^{fl}$ [56], and $Trp53^{fl}$ [57].

434 Genetic recombination was induced in mice of either sex 8-12 weeks of age by topical application to
435 the shaved backs of the mice of 100 µL tamoxifen (10 mg/ml in ethanol; T5648, Sigma) in models
436 driven by Ivl-CreERT2, or 4 µl 4-hydroxytamoxifen (20 mg/ml in ethanol; H6278, Sigma) in models
437 driven by *Krt5*-CreERT2 and *Krt14*-CreERT, unless otherwise stated. This was repeated three more
438 times over 8 days.

UV irradiation

UV irradiation experiments were conducted at the CRUK Manchester Institute husbandry facility following the UK Home Office regulations under project licences PE4369EDB and P671A5B06. In cohorts exposed to UVR, mice were subjected to UVR exposure once per week for 4 weeks, beginning 4 weeks after the final tamoxifen application. For this process, mice were anaesthetised by intraperitoneal injection with 1 mg/kg Domitor and 100 mg/kg ketamine, with 5 mg/kg Antisedan anaesthetic reversal. The backs were shaved, and a black cloth was used to cover regions that were to remain unexposed. The Waldmann UV181 unit with UV6 broad wavelength (280-380 nm) lamp was used for UVR exposure and the intensity was tested regularly with a USB2000+ spectroradiometer (Ocean Optics). The UV dose used was 0.6 kJ/m^2, which equated to 3 minutes and 14 seconds of exposure. Following irradiation, E45 moisturising cream was topically applied to the back.

Tumour fragment implantation

Tumour implantation experiments were conducted at the CRUK Manchester Institute husbandry facility following the UK Home Office regulations under project licences PE4369EDB and P671A5B06. A tumour derived from a K5:BRAF^{V600E} mouse was resected upon clinical endpoint under a laminar flow hood aseptically. The tumour was cut into 2-3 mm^3 pieces for immediate implantation on anesthetised 6-8 week-old C57/6J littermates and NSGII2 mice. Briefly, recipient animals were anesthetised with isoflurane and kept on a heated stage. A tumour piece was implanted subcutaneously between the skin and the peritoneal wall. The surgical incision was closed using a surgical clip. Rymadyl/Carprofen analgesic was given at 4mg/kg. Mice were monitored until consciousness was regained and then monitored daily. The surgical clip was removed 7 days post-surgery.

In vivo drug treatments

In vivo drug treatments were conducted at the CRUK Scotland Institute Animal Facility following the UK Home Office guidelines, under project licence PP3908577. Skin inflammation was induced by topically applying 150 µl of TPA (31.25 µg/ml) in acetone (Sigma-Aldrich 16561-29-8) to shaved dorsal skin three times per week until tumour signs appeared. The BRAFi Dabrafenib was administered by daily oral gavage (30 mg/kg in 100 µl) during the experiment.

Immunohistochemistry and immunofluorescence

Organs collected in 10% neutral buffered formalin were stored at room temperature for 20-28 hours, followed by transfer to 70% ethanol and storage at 4°C until processing. All haematoxylin and eosin (H&E), immunohistochemistry, co-immunofluorescence and *in situ* hybridisation staining were performed on 4-µm formalin-fixed paraffin-embedded sections (FFPE) which had previously been heated at 60°C for 2 hours.

472 The following antibodies were used on a Leica Bond Rx autostainer: KRT5 (905501, Biolegend), Ki67
473 (12202, Cell Signaling), SOX2 (14962, Cell Signaling) and pSTAT3 (9131, Cell Signaling). All FFPE sections
474 underwent onboard dewaxing (AR9222, Leica) and epitope retrieval using ER2 solution (AR9640, Leica)
475 for 20 minutes at 95°C. Sections were rinsed with Leica wash buffer (AR9590, Leica) before peroxidase
476 block was performed using an Intense R kit (DS9263, Leica) for 5 minutes. Sections were rinsed with
477 wash buffer before primary antibody application at an optimal dilution (KRT5, 1/1500; Ki67, 1/1000;
478 pSTAT3, 1/100; SOX2, 1/200). The sections were rinsed with wash buffer before the application of anti-
479 rabbit EnVision HRP-conjugated secondary antibody (K4003, Agilent) for 30 minutes. The sections were
480 rinsed with wash buffer, visualised using DAB, and counterstained with haematoxylin from the Intense
481 R kit.

482 FFPE sections for KRT14 (ab7800, Abcam), c-MYC (ab32072, Abcam), RFP (600-401-379, Rockland) and
483 SOX9 (AB5535, Millipore) staining were stained on an Agilent autostainer Link48. FFPE sections were
484 loaded into an Agilent pre-treatment module to be dewaxed and undergo heat-induced epitope
485 retrieval (HIER) using a High pH target retrieval solution (K8004, Agilent). After HIER, the sections were
486 rinsed in FLEX wash buffer (K8007, Agilent) before being loaded onto the Agilent autostainer. The
487 sections underwent peroxidase blocking (S2023, Agilent) for 5 minutes and were rinsed with FLEX
488 buffer. The primary antibody application was at an optimised dilution (KRT14, 1/300; c-MYC, 1/800;
489 RFP, 1/1000; SOX9, 1/500). Sections were washed with FLEX buffer before application of anti-rabbit
490 EnVision secondary antibody for 30 minutes. Sections were rinsed with FLEX wash buffer before
491 applying Liquid DAB (K3468, Agilent) for 10 minutes. Sections were washed in water and
492 counterstained with haematoxylin 'Z' (RBA-4201-00A, CellPath).

493 In-situ hybridisation detection for *Anxa1* (509298), *Ivl* (422538), *Ly6a* (427578), PPIB (313918; positive
494 control) and dapB (312038; negative control) (all Bio-Techne) mRNA was performed using RNAScope
495 2.5 LSx (Brown) detection kit (322700; Bio-Techne) according to the manufacturer's instructions. H&E
496 staining was performed on a Leica autostainer (ST5020). Sections were dewaxed in xylene, taken
497 through graded ethanol solutions and stained with haematoxylin 'Z' (RBA-4201-00A, CellPath) for 13
498 minutes. Sections were washed in water, differentiated in 1% acid alcohol, washed and the nuclei
499 stained blue in Scott's tap water substitute (in-house). After washing with tap water, sections were
500 placed in Putt's eosin (in-house) for 3 minutes. To complete H&E, IHC & ISH staining, sections were
501 rinsed in tap water, dehydrated through a series of graded alcohols, and placed in xylene. The stained
502 sections were coverslipped in xylene using DPX mountant (SEA-1300-00A, CellPath).

503 Sections for KRT14 and RFP co-IF staining were loaded onto a Leica Bond Rx autostainer. The FFPE
504 sections underwent on-board dewaxing and epitope retrieval using ER2 solution for 20 minutes at

505 95°C. Sections were rinsed with Leica wash buffer (AR9590, Leica) before application of 10% normal
506 goat serum (X090710-8, Agilent) for 30 minutes. The sections were rinsed with Leica wash buffer
507 before application of anti-RFP antibody at 1/1000 dilution for 1 hour. Sections were rinsed with Leica
508 wash buffer and goat anti-rabbit IgG 488 (A11034, Invitrogen) secondary antibody diluted 1/250 for
509 30 minutes. After rinsing with Leica wash buffer KRT14 antibody was applied at 1/750 dilution for 1
510 hour. Sections were rinsed with Leica wash buffer and goat anti-mouse IgG 647 secondary antibody
511 (A21236, Invitrogen diluted) 1/250 for 30 minutes before application of DAPI (MBD0015, Sigma-
512 Aldrich). To complete the staining, sections were mounted using ProLong Diamond antifade mountant
513 (P36970, Thermo Fisher Scientific).

514 Immunohistochemistry images were acquired using a SCN400F slide scanner (Leica Microsystems) at
515 ×20 or x40 magnification. Confocal images were collected on a Zeiss 710 point-scanning confocal
516 microscope, built on an inverted Zeiss Axio Imager.Z2 stand. Images were acquired using a EC Plan-
517 Neofluar 40x/1.30 Oil and a confocal pinhole diameter of 107 µm. Multi-channel images were
518 captured sequentially: DAPI (nuclear marker) using 405 nm excitation and 410-481 nm emission
519 bandwidth, IgG 488 using 488 nm excitation and 514-582 nm emission and IgG 647 using 633 nm
520 excitation and 638-747 nm emission. Images were collected with a 1x zoom with an image size of 2320
521 x 2320 pixels, yielding a pixel size of 92 x 92 nm, and a 1.38 us pixel dwell time. Z-stacks were collected
522 using a step size of 2 um. Images were acquired using the software Zen LSM 2.1 Black (Zeiss).

523 RNAseq sequencing and analysis

524 RNA was extracted from fresh frozen tumour samples or human cell line pellets using an AllPrep
525 DNA/RNA kit (74104, Qiagen) according to the manufacturer's instructions. Indexed poly(A) libraries
526 were prepared using 200 ng of total RNA and 14 cycles of amplification with the Agilent SureSelect
527 Strand-Specific RNA Library Preparation Kit for Illumina Sequencing (G9691B, Agilent). RNA polyA
528 libraries were sequenced using NovaSeq 6000 XP SP, 200 cycles, paired-end reads (2 x 101 bp) 20-30
529 million reads. RNA preparation and sequencing of mouse samples were performed at the CRUK
530 Manchester Institute histology core and sequencing facility. RNA preparation and sequencing of
531 human cell lines were performed at GENEWIZ Azenta.

532 For mouse samples raw sequence quality control was performed using FastQC (v0.11.8) before and
533 after removing adapters and low-quality base calls (Phred score <20) using TrimGalore with default
534 options (v0.6.6). Trimmed reads were aligned to GRCm38, release 100 using Hisat2 (v2.1.0). Gene
535 counts were subsequently estimated using featurecounts (subread/1.6.3). For human cell lines, raw
536 sequence quality control and alignment were performed using Nextfow nf-core/rnaseq pipeline using
537 STAR and Salmon [58]. Trimmed reads were aligned to GRCh38, release 113. Sva::ComBat-seq was used

538 for batch correction (v3.52.0). For all samples, after removing transcripts without a minimum of 5
539 reads in at least one sample, the differential expression analysis between mouse tumours and skin was
540 performed using the R package DESeq2 (v1.44.0). The resultant p-values were corrected for multiple
541 comparisons using the Benjamini-Hochberg approach. The following additional R packages were used
542 for downstream analysis: pheatmap (v1.0.8), fgsea (v1.30.0), enhancedVolcano (v1.22.0),
543 clusterProfiler (v4.12.6), dplyr (v1.1.4), tidyr (v1.3.1), AnnotationHub (v3.12.0), ggvenn (0.1.10),
544 AnnotationDbi (v1.66.0), mixOmics (v6.26.0).

545 Culture of human keratinocyte cell lines and introduction of genetic modifications

546 Human keratinocyte cell lines were maintained in serum-free Keratinocyte Growth Medium 2 (C-
547 20011, PromoCell) until confluent and then split using 0.25% Trypsin-EDTA (T4049-100ML, Merck) and
548 quenched using Defined Trypsin Inhibitor (R007100, Gibco). All cell culture incubators were set to 37°C
549 and 5% CO2.

550 Normal human primary juvenile keratinocytes (JHEK) (C-12006, PromoCell) and normal human primary
551 adult keratinocytes (AHEK) (102-05a, Cell Applications) were immortalised with in-house produced
552 lentivirus expressing the hTERT-hygromycin resistant pLV-EF1a-IRES-Hygro plasmid and selected with
553 hygromycin (300 µg/ml). The plasmid was a gift from Tobias Meyer (85140, Addgene) [59]). Then,
554 nucleofection-based CRISPR-Cas-9 methodology was used to generate p16 KO using the 4D
555 Nucleofector Core Unit (AAF-1002B with AAF-1002X, Lonza). A gRNA with enhanced stability targeting
556 *Cdkn2a* (p16) was designed and purchased from Integrated DNA Technologies (IDT). Ribonucleoprotein
557 (RNP) complexes were formed by diluting 120 pmol sgRNA, 104 pmol Cas9 Nuclease V3 (1081059,
558 IDT), 1 µl of Alt-R Cas9 Electroporation Enhancer (1075916, IDT) in Nuclease-Free IDTE, pH 7.5 (1X TE
559 solution) (I11-01-02-02, IDT). RNP complex was added to 20 µl of Primary Cell P3 Nucleofector Solution
560 (V4XP-3032, Lonza) and nucleofected using programme CM137. The mixture was then transferred to
561 a 20 µl nucleocuvette strip and nucleofected using programme CM137. The targeted sequence was
562 PCR-amplified, sequenced at Eurofins and KO-validated using the TIDE algorithm (achieving >90%
563 efficiency)[60]. *SOX2* overexpression lentivirus with puromycin resistance was purchased from
564 VectorBuilder ready-to-use (vector id VB900088-3008dcy). SOX2-overexpressing keratinocytes were
565 selected with 1 µg/ml puromycin. GFP overexpression control lentivirus with puromycin resistance
566 purchased from VectorBuilder ready-to-use were used as controls. Cell pellets were regularly collected
567 and submitted for cell line authentication at Eurofins and tested for Mycoplasma in-house.

568 Immunoblotting

569 Proteins were extracted from whole-cell lysates using RIPA buffer (R0278, Sigma-Aldrich) mixed with 1
570 tablet of cOmplete™ Protease Inhibitor Cocktail (11873580001, Sigma-Aldrich). Cell suspensions were

571 incubated on ice for 10 minutes before centrifuging at 13,000 rpm for 10 minutes at 4°C. Protein
572 extracts from the supernatants were quantified using the Pierce™ BCA Protein Assay Kit (23225,
573 Invitrogen). Protein extracts (25 µg) were denatured in 4x Laemmli sample buffer (1610747, BIO-RAD)
574 at 95 °C for 5 minutes. The samples were separated on NuPAGE™ 4-12% Bis-Tris Mini Protein Gels
575 (NP0322BOX, Invitrogen) at 120 V for 1 hour in 1x MOPS SDS running buffer (B0001, Invitrogen)
576 together with the Chameleon Duo pre-stained Protein Ladder (928-60000, LI-COR). The proteins were
577 transferred onto a nitrocellulose membrane (170-4270, BIO-RAD), using the BIO-RAD Trans-Blot Turbo
578 Transfer System. The membrane was blocked with 1x TBST with 5% BSA (A7906, Sigma-Aldrich) for 1
579 hour at room temperature in the dark. The membrane was then incubated in anti-SOX2 antibody
580 1:1000 (23064, Cell Signalling) and anti-β-actin 1:10,000 (MA1-140, Invitrogen) diluted in 1x TBST 5%
581 BSA, at 4°C overnight in the dark. β-actin was used as a loading control. Followed by 3x10 minute
582 washes in 1x TBST in the dark and subsequently incubated in fluorescence-conjugated secondary
583 antibodies, diluted in 5% BSA in 1x TBST, at room temperature for 45 minutes in the dark. Secondary
584 antibodies used were anti-rabbit IgG (A32735, Thermo Fisher Scientific) and anti-mouse IgG
585 (A21057, Thermo Fisher Scientific). This was followed by 3x10 minute washes in 1x TBST before the
586 membrane was scanned using the LI-COR Odyssey® CLx Infrared Imaging System.

587 ## Data availability

588 The data discussed in this publication will be deposited in NCBI's Gene Expression Omnibus.

589 # ACKNOWLEDGMENTS

590 We thank the Core Services and Advanced Technologies at the Cancer Research UK Scotland and
591 Manchester Institutes, particularly the Biological Services Unit, Histology Service and Molecular
592 Technologies. We thank Gareth Inman for the useful discussion (Cancer Research UK Scotland
593 Institute). We also thank Claire Mitchell and the BAIR Biological Advance Image Resource service at
594 Cancer Research UK Scotland Institute. We thank Kevin Haigis (Dana-Farber Cancer Institute) for
595 providing the HRAS^{G12V} mouse model. We are grateful to Sarah Ressel for the critical review of the
596 manuscript and Nathalie Sphyris for expert writing advice (Cancer Research UK Scotland Institute). This
597 work was supported by Cancer Research UK Cancer Grand Challenges and The Mark Foundation for
598 Cancer Research to the SPECIFICANCER team (A29055) and by CRUK core funding to the Cancer
599 Research UK Manchester Institute (C5759/A27412) and the Cancer Research UK Scotland Institute
600 (C5759/A31287). P.P.C. and C.C. were funded by the Cancer Research UK Grand Challenge
601 SPECIFICANCER Consortium (A29055 & A27412). C.A.F, R.A.R., P.C., T.J, O.J.S. were supported by CRUK
602 Beatson Institute core funding (A17196, A31287).

AUTHOR CONTRIBUTIONS

P.P.C., A.C., R.M. and O.J.S. designed experiments and interpreted results. P.PC, C.C., C.A.F., R.A.R., T.J.S. and P.C. performed experiments and analysed results. P.P.C. analysed publicly available human cancer data sets. P.P.C. processed and analysed the RNA sequencing data. P.PC., A.C. and O.J.S. wrote the paper, and reviewed and discussed the drafted manuscript. All authors contributed to the manuscript.

REFERENCES

1. Martincorena I, Roshan A, Gerstung M, et al. High burden and pervasive positive selection of somatic mutations in normal human skin. *Science (1979)*. 2015;348(6237):880-886. doi:10.1126/science.aaa6806

2. Taylor MA, Kandyba E, Halliwill K, et al. Stem-cell states converge in multistage cutaneous squamous cell carcinoma development. *Science*. 2024;384(6699):eadi7453. doi:10.1126/SCIENCE.ADI7453

3. Chang D, Shain AH. The landscape of driver mutations in cutaneous squamous cell carcinoma. *NPJ Genom Med*. 2021;6(1):61. doi:10.1038/s41525-021-00226-4

4. Ge Y, Gomez NC, Adam RC, Yuan S, Elemento O, Fuchs Correspondence E. Stem Cell Lineage Infidelity Drives Wound Repair and Cancer. *Cell*. 2017;169:636-650. doi:10.1016/j.cell.2017.03.042

5. Bernabé-Rubio M, Ali S, Bhosale PG, et al. Myc-dependent dedifferentiation of Gata6+ epidermal cells resembles reversal of terminal differentiation. *Nature Cell Biology 2023*. Published online September 21, 2023:1-13. doi:10.1038/s41556-023-01234-5

6. Aragona M, Sifrim A, Malfait M, et al. Mechanisms of stretch-mediated skin expansion at single-cell resolution. *Nature 2020 584:7820*. 2020;584(7820):268-273. doi:10.1038/s41586-020-2555-7

7. Lapouge G, Youssef KK, Vokaer B, et al. Identifying the cellular origin of squamous skin tumors. *Proceedings of the National Academy of Sciences*. 2011;108(18):7431-7436. doi:10.1073/pnas.1012720108

8. Kretzschmar K, Weber C, Driskell RR, Calonje E, Watt FM. Compartmentalized Epidermal Activation of β-Catenin Differentially Affects Lineage Reprogramming and Underlies Tumor Heterogeneity. *Cell Rep*. 2016;14(2):269-281. doi:10.1016/J.CELREP.2015.12.041

9. Cammareri P, Rose AM, Vincent DF, et al. Inactivation of TGFβ receptors in stem cells drives cutaneous squamous cell carcinoma. *Nat Commun*. 2016;7(1):12493. doi:10.1038/ncomms12493

10. Mascré G, Dekoninck S, Drogat B, et al. Distinct contribution of stem and progenitor cells to epidermal maintenance. *Nature*. 2012;489(7415):257-262. doi:10.1038/nature11393

11. Sarate RM, Hochstetter J, Valet M, et al. Dynamic regulation of tissue fluidity controls skin repair during wound healing. *Cell*. 2024;187. doi:10.1016/j.cell.2024.07.031

641 12. Cockburn K, Annusver K, Gonzalez DG, et al. Gradual differentiation uncoupled from
642 cell cycle exit generates heterogeneity in the epidermal stem cell layer. *Nature Cell*
643 *Biology 2022 24:12*. 2022;24(12):1692-1700. doi:10.1038/s41556-022-01021-8

644 13. Quintanilla M, Brown K, Ramsden M, Balmain A. Carcinogen-specific mutation and
645 amplification of Ha-ras during mouse skin carcinogenesis. *Nature 1986 322:6074*.
646 1986;322(6074):78-80. doi:10.1038/322078a0

647 14. Nassar D, Latil M, Boeckx B, Lambrechts D, Blanpain C. Genomic landscape of
648 carcinogen-induced and genetically induced mouse skin squamous cell carcinoma. *Nat*
649 *Med*. 2015;21(8):946-954. doi:10.1038/nm.3878

650 15. Oberholzer PA, Kee D, Dziunycz P, et al. RAS Mutations Are Associated With the
651 Development of Cutaneous Squamous Cell Tumors in Patients Treated With RAF
652 Inhibitors. *Journal of Clinical Oncology*. 2012;30(3):316-321.
653 doi:10.1200/JCO.2011.36.7680

654 16. Hauschild A, Grob JJ, Demidov L V., et al. Dabrafenib in BRAF-mutated metastatic
655 melanoma: A multicentre, open-label, phase 3 randomised controlled trial. *The Lancet*.
656 Published online 2012. doi:10.1016/S0140-6736(12)60868-X

657 17. Su F, Viros A, Milagre C, et al. *RAS Mutations in Cutaneous Squamous-Cell Carcinomas*
658 *in Patients Treated with BRAF Inhibitors A Bs t r Ac t*. Vol 366.; 2012. doi:2012;366:207-
659 15

660 18. Poulikakos PI, Zhang C, Bollag G, Shokat KM, Rosen N. RAF inhibitors transactivate RAF
661 dimers and ERK signalling in cells with wild-type BRAF. *Nature*. 2010;464(7287):427-
662 430. doi:10.1038/nature08902

663 19. Bailey P, Ridgway RA, Cammareri P, et al. Driver gene combinations dictate cutaneous
664 squamous cell carcinoma disease continuum progression. *Nat Commun*.
665 2023;14(1):5211. doi:10.1038/S41467-023-40822-9

666 20. White AC, Tran K, Khuu J, et al. Defining the origins of Ras/p53-mediated squamous
667 cell carcinoma. *Proceedings of the National Academy of Sciences*. 2011;108(18):7425-
668 7430. doi:10.1073/pnas.1012670108

669 21. Vanzan L, Soldati H, Ythier V, et al. High throughput screening identifies SOX2 as a
670 super pioneer factor that inhibits DNA methylation maintenance at its binding sites.
671 *Nat Commun*. 2021;12(1):3337. doi:10.1038/s41467-021-23630-x

672 22. Joost S, Jacob T, Sun X, et al. Single-Cell Transcriptomics of Traced Epidermal and Hair
673 Follicle Stem Cells Reveals Rapid Adaptations during Wound Healing. *Cell Rep*.
674 2018;25(3):585-597.e7. doi:10.1016/J.CELREP.2018.09.059

675 23. Sennett R, Wang Z, Rezza A, et al. An Integrated Transcriptome Atlas of Embryonic Hair
676 Follicle Progenitors, Their Niche, and the Developing Skin. *Dev Cell*. 2015;34(5):577-
677 591. doi:10.1016/J.DEVCEL.2015.06.023

678 24. Ji AL, Rubin AJ, Thrane K, et al. Multimodal Analysis of Composition and Spatial
679 Architecture in Human Squamous Cell Carcinoma. *Cell*. 2020;182(2):497-514.e22.
680 doi:10.1016/j.cell.2020.05.039

681 25. Zou DD, Sun YZ, Li XJ, et al. Single-cell sequencing highlights heterogeneity and
682 malignant progression in actinic keratosis and cutaneous squamous cell carcinoma.
683 *Elife*. 2023;12. doi:10.7554/eLife.85270

684 26. Bizzarro V, Belvedere R, Milone MR, et al. Annexin A1 is involved in the acquisition and
685 maintenance of a stem cell-like/aggressive phenotype in prostate cancer cells with
686 acquired resistance to zoledronic acid. *Oncotarget*. 2015;6(28):25074.
687 doi:10.18632/ONCOTARGET.4725

688 27. Al-Ali HN, Crichton SJ, Fabian C, et al. A therapeutic antibody targeting annexin-A1
689 inhibits cancer cell growth in vitro and in vivo. *Oncogene 2024 43:8*. 2024;43(8):608-
690 614. doi:10.1038/s41388-023-02919-9

691 28. Yui S, Azzolin L, Maimets M, et al. YAP/TAZ-Dependent Reprogramming of Colonic
692 Epithelium Links ECM Remodeling to Tissue Regeneration. *Cell Stem Cell*.
693 2018;22(1):35-49.e7. doi:10.1016/J.STEM.2017.11.001

694 29. Gil Vazquez E, Nasreddin N, Valbuena GN, et al. Dynamic and adaptive cancer stem cell
695 population admixture in colorectal neoplasia. *Cell Stem Cell*. 2022;29(8):1213-1228.e8.
696 doi:10.1016/j.stem.2022.07.008

697 30. Liu S, Hur YH, Cai X, et al. A tissue injury sensing and repair pathway distinct from host
698 pathogen defense. *Cell*. 2023;186(10):2127-2143.e22. doi:10.1016/j.cell.2023.03.031

699 31. Johnson BZ, Stevenson AW, Prêle CM, Fear MW, Wood FM. The Role of IL-6 in Skin
700 Fibrosis and Cutaneous Wound Healing. *Biomedicines 2020, Vol 8, Page 101*.
701 2020;8(5):101. doi:10.3390/BIOMEDICINES8050101

702 32. Boumahdi S, de Sauvage FJ. The great escape: tumour cell plasticity in resistance to
703 targeted therapy. *Nat Rev Drug Discov*. 2020;19(1):39-56. doi:10.1038/s41573-019-
704 0044-1

705 33. Siegle JM, Basin A, Sastre-Perona A, et al. SOX2 is a cancer-specific regulator of tumour
706 initiating potential in cutaneous squamous cell carcinoma. *Nat Commun*. 2014;5.
707 doi:10.1038/NCOMMS5511

708 34. Yang Y, Gomez N, Infarinato N, et al. The pioneer factor SOX9 competes for epigenetic
709 factors to switch stem cell fates. *Nature Cell Biology 2023*. Published online July 24,
710 2023:1-11. doi:10.1038/s41556-023-01184-y

711 35. Boumahdi S, Driessens G, Lapouge G, et al. SOX2 controls tumour initiation and cancer
712 stem-cell functions in squamous-cell carcinoma. *Nature*. 2014;511(7508):246-250.
713 doi:10.1038/NATURE13305

714 36. Gallini S, Annusver K, Rahman NT, et al. Injury prevents Ras mutant cell expansion in
715 mosaic skin. *Nature 2023*. Published online June 21, 2023:1-9. doi:10.1038/s41586-
716 023-06198-y

717 37. Vermeulen L, Morrissey E, Van Der Heijden M, et al. Defining stem cell dynamics in
718 models of intestinal tumor initiation. *Science*. 2013;342(6161):995-998.
719 doi:10.1126/SCIENCE.1243148

720 38. Sabnis AJ, Cheung LS, Dail M, et al. Oncogenic Kras initiates leukemia in hematopoietic
721 stem cells. Jordan CT, ed. *PLoS Biol*. 2009;7(3):e1000059.
722 doi:10.1371/JOURNAL.PBIO.1000059

723 39. Frede J, Greulich P, Nagy T, Simons BD, Jones PH. A single dividing cell population with
724 imbalanced fate drives oesophageal tumour growth. *Nat Cell Biol*. 2016;18(9):967-978.
725 doi:10.1038/ncb3400

726 40. Schaefer T, Lengerke C. SOX2 protein biochemistry in stemness, reprogramming, and
727 cancer: the PI3K/AKT/SOX2 axis and beyond. *Oncogene 2019 39:2*. 2019;39(2):278-
728 292. doi:10.1038/s41388-019-0997-x

729 41. Cammareri P, Vincent DF, Hodder MC, et al. TGFβ pathway limits dedifferentiation
730 following WNT and MAPK pathway activation to suppress intestinal tumourigenesis.
731 *Cell Death Differ*. 2017;24(10):1681-1693. doi:10.1038/CDD.2017.92

732 42. Sastre-Perona A, Hoang-Phou S, Leitner MC, Okuniewska M, Meehan S, Schober M. De
733 Novo PITX1 Expression Controls Bi-Stable Transcriptional Circuits to Govern Self-
734 Renewal and Differentiation in Squamous Cell Carcinoma. *Cell Stem Cell*.
735 2019;24(3):390-404.e8. doi:10.1016/j.stem.2019.01.003

736 43. Wu Z, Zhou J, Zhang X, et al. Reprogramming of the esophageal squamous carcinoma
737 epigenome by SOX2 promotes ADAR1 dependence. *Nat Genet*. 2021;53(6):881-894.
738 doi:10.1038/s41588-021-00859-2

739 44. Jiang YY, Jiang Y, Li CQ, et al. TP63, SOX2, and KLF5 Establish a Core Regulatory Circuitry
740 That Controls Epigenetic and Transcription Patterns in Esophageal Squamous Cell
741 Carcinoma Cell Lines. *Gastroenterology*. 2020;159(4):1311-1327.e19.
742 doi:10.1053/j.gastro.2020.06.050

743 45. Punovuori K, Bertillot F, Miroshnikova YA, Mä A, Ivaska J, Wickströ M Correspondence
744 SA. Multiparameter imaging reveals clinically relevant cancer cell-stroma interaction
745 dynamics in head and neck cancer. *Cell*. Published online 2024.
746 doi:10.1016/j.cell.2024.09.046

747 46. Van Keymeulen A, Rocha AS, Ousset M, et al. Distinct stem cells contribute to
748 mammary gland development and maintenance. *Nature*. 2011;479(7372):189-193.
749 doi:10.1038/nature10573

750 47. Vasioukhin V, Degenstein L, Wise B, Fuchs E. The magical touch: Genome targeting in
751 epidermal stem cells induced by tamoxifen application to mouse skin. *Proc Natl Acad*
752 *Sci U S A*. 1999;96(15):8551-8556. doi:10.1073/pnas.96.15.8551

753 48. Mercer K, Giblett S, Green S, et al. Expression of endogenous oncogenic V600EB-raf
754 induces proliferation and developmental defects in mice and transformation of
755 primary fibroblasts. *Cancer Res*. 2005;65(24):11493-11500. doi:10.1158/0008-
756 5472.CAN-05-2211

757 49. Dhomen N, Reis-Filho JS, da Rocha Dias S, et al. Oncogenic Braf Induces Melanocyte
758 Senescence and Melanoma in Mice. *Cancer Cell*. 2009;15(4):294-303.
759 doi:10.1016/j.ccr.2009.02.022

760 50. Bender RHF, Haigis KM, Gutmann DH. Activated k-ras, but not h-ras or N-ras, regulates
761 brain neural stem cell proliferation in a raf/rb-dependent manner. *Stem Cells*.
762 2015;33(6):1998-2010. doi:10.1002/STEM.1990

763 51. Madisen L, Zwingman TA, Sunkin SM, et al. A robust and high-throughput Cre reporting
764 and characterization system for the whole mouse brain. *Nat Neurosci*. 2010;13(1):133-
765 140. doi:10.1038/NN.2467

766 52. Shaham O, Smith AN, Robinson ML, Taketo MM, Lang RA, Ashery-Padan R. Pax6 is
767 essential for lens fiber cell differentiation. *Development*. 2009;136(15):2567-2578.
768 doi:10.1242/DEV.032888

769 53. Lu Y, Futtner C, Rock JR, et al. Evidence That SOX2 Overexpression Is Oncogenic in the
770 Lung. *PLoS One*. 2010;5(6):e11022. doi:10.1371/JOURNAL.PONE.0011022

771 54. Barker N, Van Es JH, Kuipers J, et al. Identification of stem cells in small intestine and
772 colon by marker gene Lgr5. *Nature 2007 449:7165*. 2007;449(7165):1003-1007.
773 doi:10.1038/nature06196

774 55. Jackson EL, Willis N, Mercer K, et al. Analysis of lung tumor initiation and progression
775 using conditional expression of oncogenic K-ras. *Genes Dev*. 2001;15(24):3243-3248.
776 doi:10.1101/GAD.943001

777 56. McCright B, Lozier J, Gridley T. Generation of new Notch2 mutant alleles. *Genesis*.
778 2006;44(1):29-33. doi:10.1002/GENE.20181

779 57. Jonkers J, Meuwissen R, Van der Gulden H, Peterse H, Van der Valk M, Berns A.
780 Synergistic tumor suppressor activity of BRCA2 and p53 in a conditional mouse model
781 for breast cancer. *Nat Genet*. 2001;29(4):418-425. doi:10.1038/NG747

782 58. Ewels PA, Peltzer A, Fillinger S, et al. The nf-core framework for community-curated
783 bioinformatics pipelines. *Nature Biotechnology 2020 38:3*. 2020;38(3):276-278.
784 doi:10.1038/s41587-020-0439-x

785 59. Hayer A, Shao L, Chung M, et al. Engulfed cadherin fingers are polarized junctional
786 structures between collectively migrating endothelial cells. *Nat Cell Biol*.
787 2016;18(12):1311. doi:10.1038/NCB3438

788 60. Brinkman EK, Chen T, Amendola M, Van Steensel B. Easy quantitative assessment of
789 genome editing by sequence trace decomposition. *Nucleic Acids Res*.
790 2014;42(22):e168-e168. doi:10.1093/NAR/GKU936

791

792

FIGURES

Figure 1

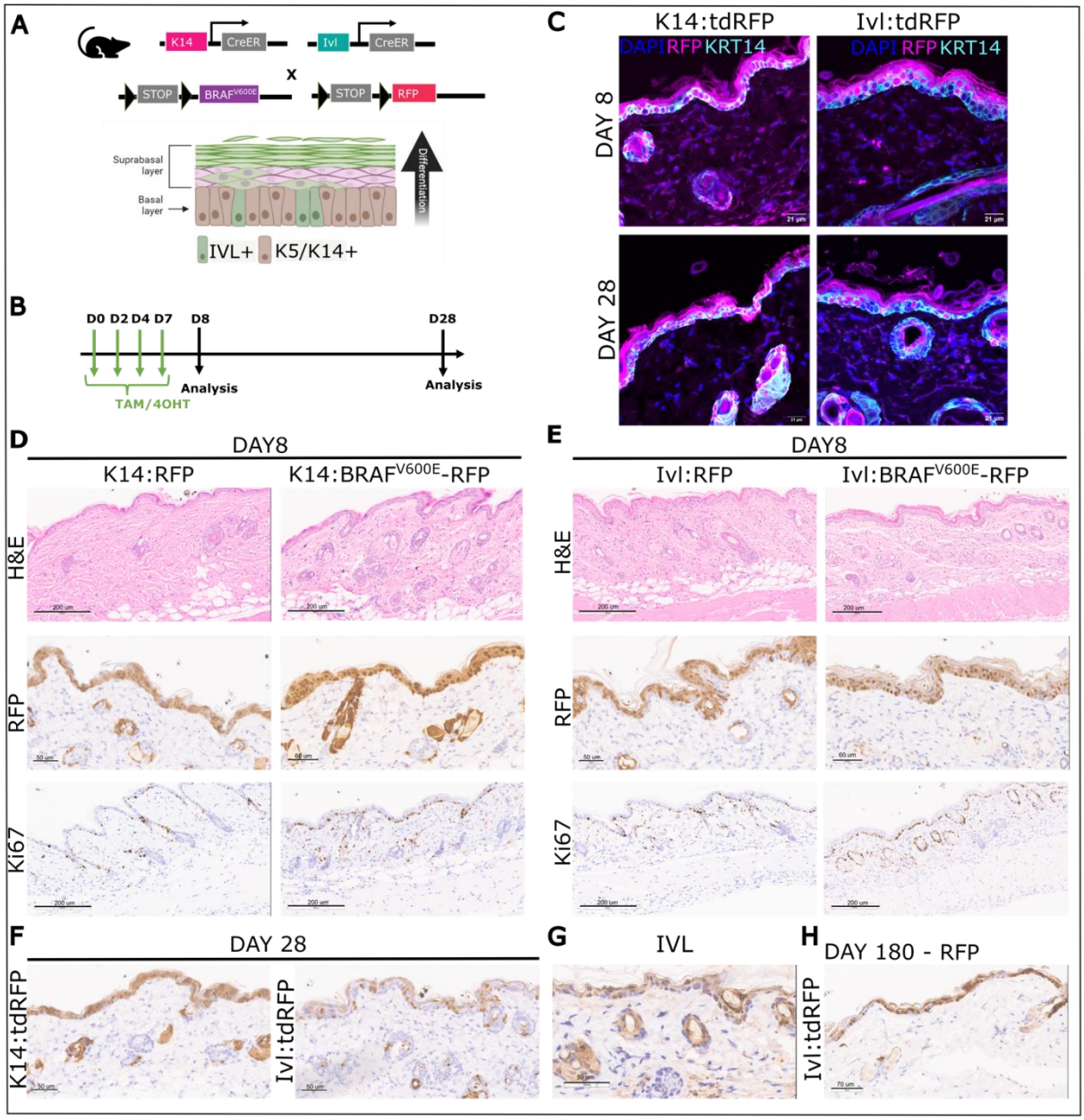

Figure 1. **Distinct basal populations coexist in the epidermis and compete upon BRAF^{V600E} expression.** **A,** Schematic representation of the mouse models used for lineage tracing (top) and the epidermis (bottom) formed by the suprabasal, formed by IVL+ cells, and the basal layer, which includes a mixture of K14+/K5+ and IVL+ cells. **B,** Schematic representation of the experimental design used for tamoxifen induction of Cre-mediated recombination and lineage tracing. **C,** Representative Z-stack co-immunofluorescence (IF) of KRT14 and RFP at day 8 and day 28 post tdRFP induction in K14:tdRFP and

801 Ivl:tdRFP normal skin. **D and E**, Representative H&E and immunohistochemistry (IHC) of RFP and Ki67
802 conducted in skin at day 8 post-induction from K14:tdRFP and K14:BRAF^{V600E}-tdRFP (D) and Ivl:tdRFP
803 and Ivl:BRAF^{V600E}-tdRFP (E) models. **F**, Representative images of IHC of RFP performed in K14:tdRFP
804 and Ivl:tdRFP normal skin at day 28 post induction. **G,** Representative image of IHC of IVL staining in
805 wild-type skin showing positive cells in the basal and suprabasal layers. **H,** Representative IHC of RFP
806 from Ivl:tdRFP normal skin at 180 days post tdRFP induction showing label-retaining populations
807 residing in the basal layer.

808

Figure 2

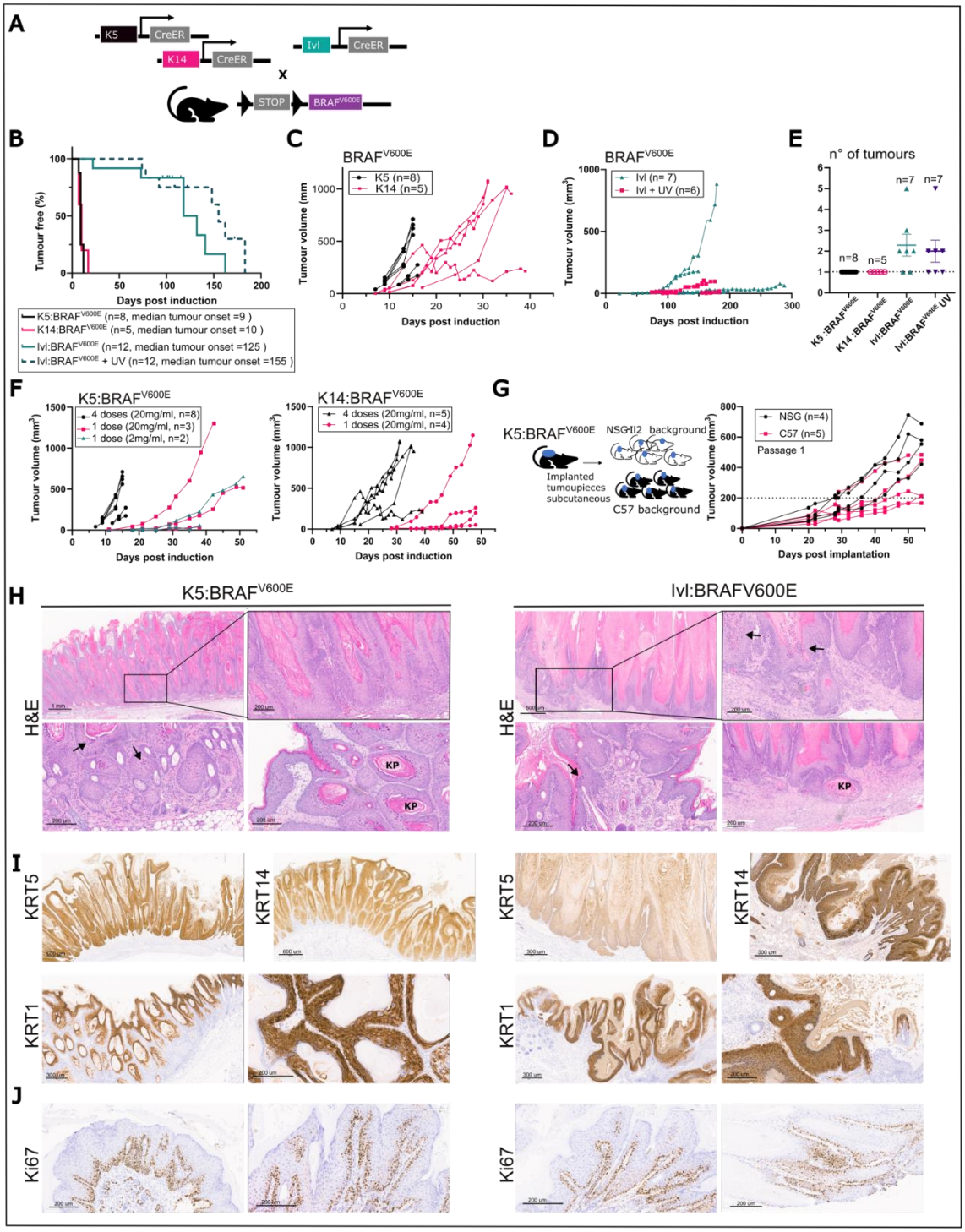

Figure 2. Tumour-primed and tumour-resistant populations coexist in the basal layer. A, Schematic representation of the mouse models used for skin tumorigenesis. **B,** Kaplan-Meier plot displaying tumour-free survival for K5:BRAF^{V600E}, K14:BRAF^{V600E}, Ivl:BRAF^{V600E}, and Ivl:BRAF^{V600E}+ UV-treated female mice aged until clinical endpoint. **C, D and E**, Total tumour growth in K5:BRAF^{V600E} and K14:BRAF^{V600E} (C) and in Ivl:BRAF^{V600E} and UV-treated Ivl:BRAF^{V600E} (D) female mice and total tumour number (Mean and SEM) (E) in female mice aged until clinical endpoint. **F,** Tumour burden growth at

816 different induction regimens in K5:BRAF^{V600E} and K14:BRAF^{V600E} models. **G,** Schematic and tumour
817 burden growth of K5:BRAF^{V600E} tumour pieces transplanted into C57/6J and immunosuppressed
818 female mice (NSG-II2). **H, I and J**, Representative images of K5:BRAF^{V600E} (left) and Ivl:BRAF^{V600E} (right)
819 tumours showing H&E staining (H) and IHC of skin hierarchy markers KRT5, KRT14 and KRT1 (I), and
820 proliferation marker Ki67 (J) at clinical endpoint. Keratin pearls are indicated (KP) and arrows indicate
821 nuclear atypia.

822

Figure 3

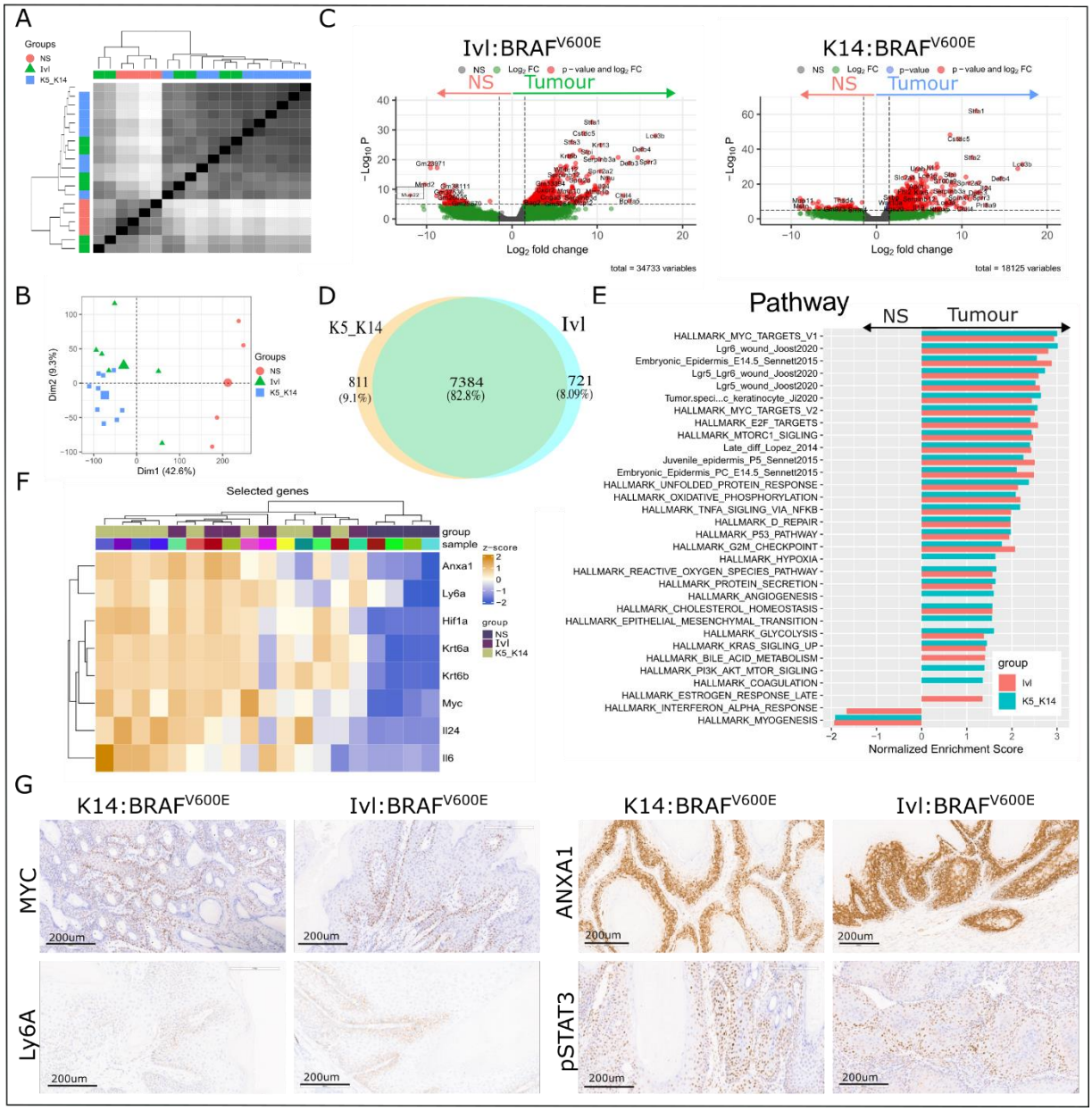

Figure 3. Transcriptional landscape of tumours derived from primed K5/K14:BRAF^{V600E} and resistant Ivl:BRAF^{V600E} basal populations. **A and B**, Hierarchical clustering heatmap (A) and principal component analysis (PCA)(B) of normalised expression values showing the correlation between the transcriptional profiles of normal skin (NS, n=4), Ivl:BRAF^{V600E} (IVL, n=6) and K5/K14:BRAF^{V600E} (K5_K14, n=9). **C**, Volcano plots showing differentially expressed genes in IVL tumours (left) and K5_K14 tumours (right) compared with normal skin using the Wald test (two-tailed). **D,** Venn diagram showing upregulated genes shared between Ivl:BRAF^{V600E} (Ivl) and K5/K14:BRAF^{V600E} (K5_K14) tumours compared to normal skin. **E,** Gene set enrichment analysis of Hallmarks and indicated pathways in K5_K14 tumours and IVL tumours. Showing pathways significantly enriched (padj<0.01 based on an adaptive multi-level split Monte-Carlo). **F,** Hierarchical clustering heatmap of selected genes showing normalised expression and correlation between normal skin (NS), Ivl:BRAF^{V600E} (Ivl) and K5/K14:BRAF^{V600E}

834 (K5_K14). **G,** Representative images of IHC validation of selected targets in K14:BRAF^{V600E} and Ivl:BRAF^{V600E}
835 tumours at the clinical endpoint.
836

Figure 4

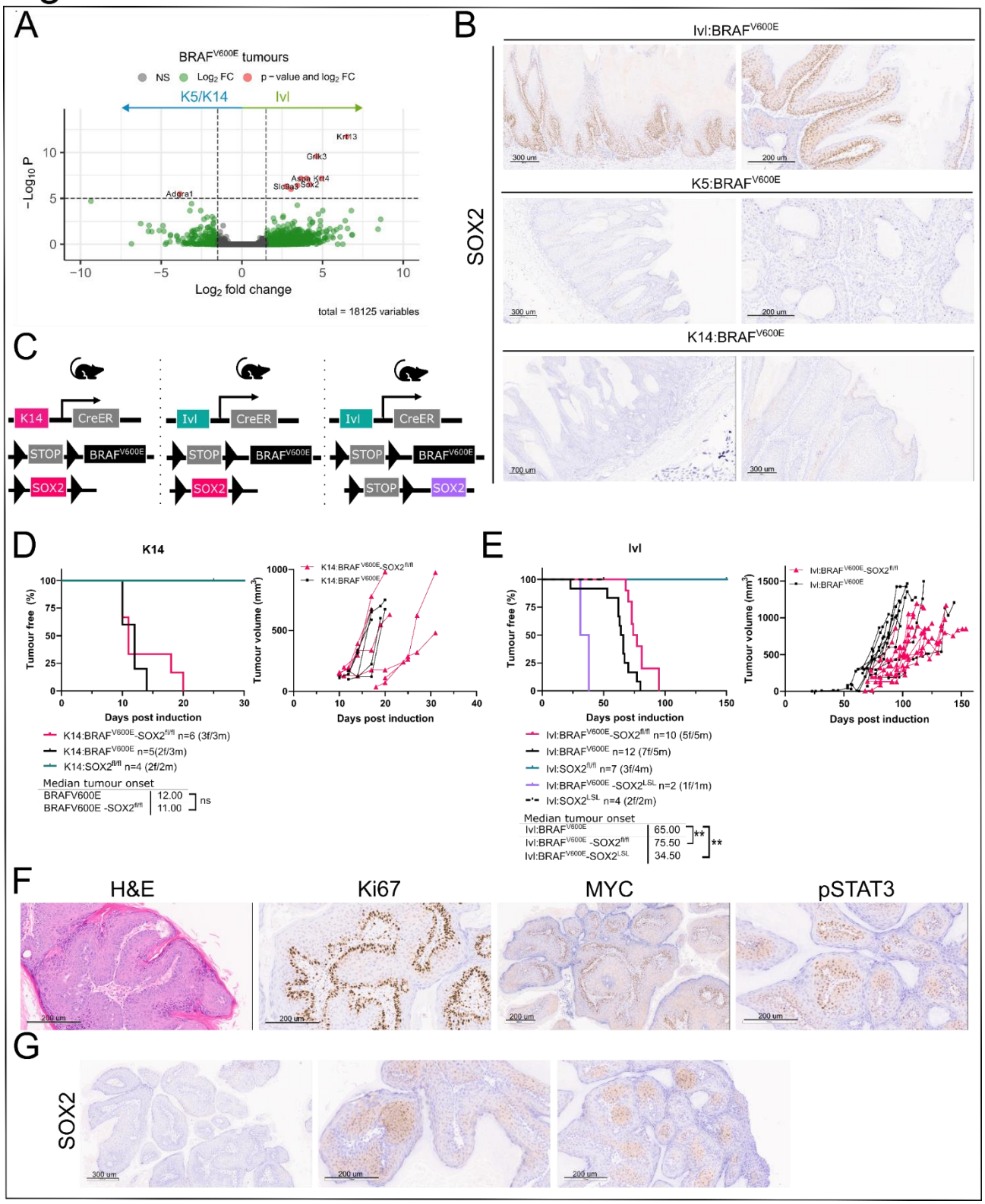

Figure 4. The tumour-resistant basal population depends on SOX2 for transformation. A, Volcano plot showing differentially expressed genes between K5/K14:BRAF^{V600E} and Ivl:BRAF^{V600E} tumours using Wald test (two-tailed). **B,** Representative images of IHC validation of SOX2 in Ivl:BRAF^{V600E} ,

841 K5:BRAF^{V600E}, and K14:BRAF^{V600E} tumours at clinical endpoint. **C,** Schematic representation of the
842 mouse models used for tumorigenesis. **D and E**, Kaplan-Meier tumour-free survival plot and tumour
843 growth for K14:BRAF^{V600E}, K14:BRAF^{V600E}-SOX2$^{fl/fl}$ and K14:SOX2$^{fl/fl}$ (D) and for Ivl:BRAF^{V600E},
844 Ivl:BRAF^{V600E}-SOX2$^{fl/fl}$ and Ivl:SOX2$^{fl/fl}$(E). P-values were determined using the log-rank (Mantel-Cox)
845 test. NS, not significant P>0.05, ** p<0.01. Note that K14:BRAF^{V600E} and Ivl:BRAF^{V600E} cohorts
846 correspond to CRUK-SI cohorts shown in Figure 1D and F and are shown here for comparison. **F,**
847 Representative H&E and IHC of Ki67, MYC and pSTAT3 in Ivl:BRAF^{V600E}-SOX2$^{fl/fl}$ tumour at the clinical
848 endpoint. **G,** IHC validation of SOX2 expression in Ivl:BRAF^{V600E}-SOX2$^{fl/fl}$ tumours revealing partial
849 expression of SOX2.

850

Figure 5

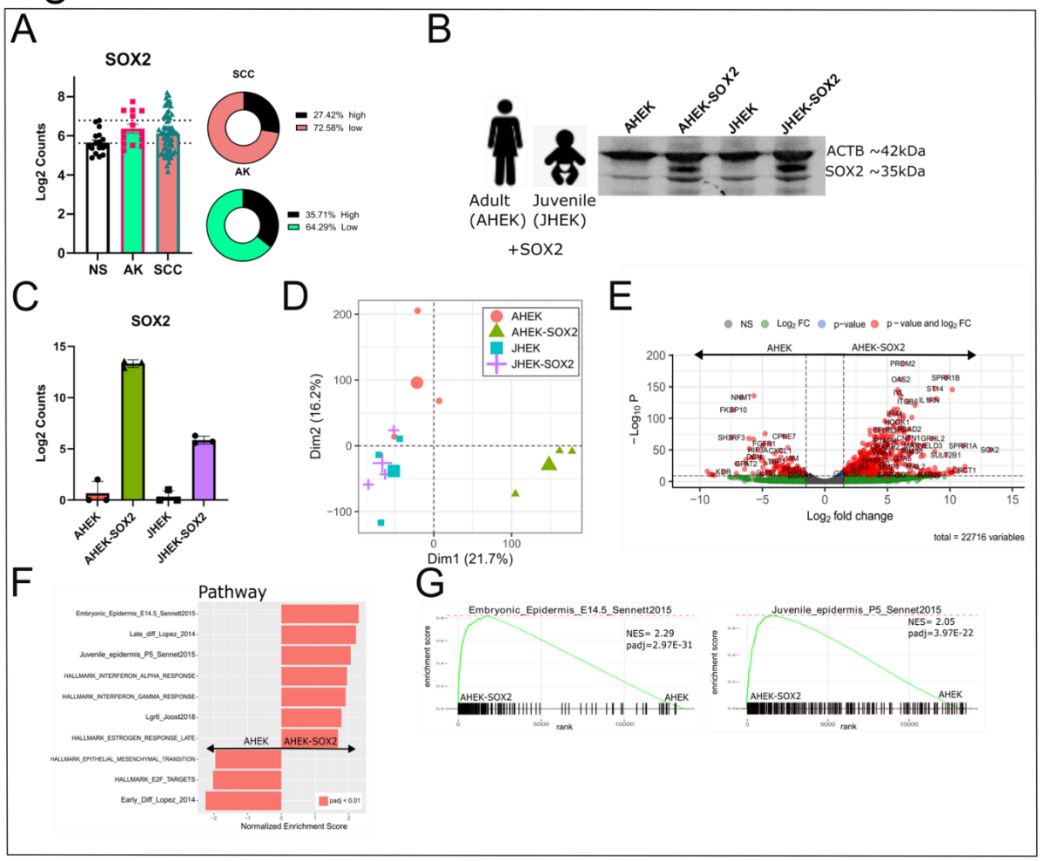

Figure 5. cSCC patients express SOX2 and it drives embryonic and juvenile signatures. A, Normalised RNA expression levels (counts) of SOX2 from a cSCC human dataset [19] including normal skin (NS, n=17), and different levels of disease progression including actinic keratosis (AK, n=14) and cutaneous squamous cell carcinoma (SCC, n=66). Dotted lines mark the mean *SOX2* normalised expression in normal skin and two standard deviations from the mean. Pie charts showing the percentage of samples with high and low *SOX2* normalised expression for SCC and AK groups. Two standard deviations from normal skin mean were used as a threshold. **B,** Western-blot validation of SOX2 overexpression in adult (AHEK) and juvenile (JHEK) human keratinocytes. **C,** Normalised RNA expression levels (counts) of SOX2 in AHEK, JHEK, and SOX2-overexpressing AHEK-SOX2 and JHEK-SOX2. N=3, repeated independent experiments per group. **D,** Principal component analysis (PCA) of normalised expression values showing the correlation between the transcriptional profiles of JHEK, JHEK-SOX2, AHEK, and AHEK-SOX2. N=3, repeated independent experiments per group. **E,** Volcano plot showing differentially expressed genes between AHEK and AHEK-SOX2 using the Wald test (two-tailed). **F,** Gene set enrichment analysis of Hallmarks and indicated pathways in AHEK and AHEK-SOX2. Pathways are significantly enriched (padj<0.01 based on an adaptive multi-level split Monte-Carlo). **G,** Normalised enriched scores of embryonic and juvenile epidermis signatures [23].

Figure 6

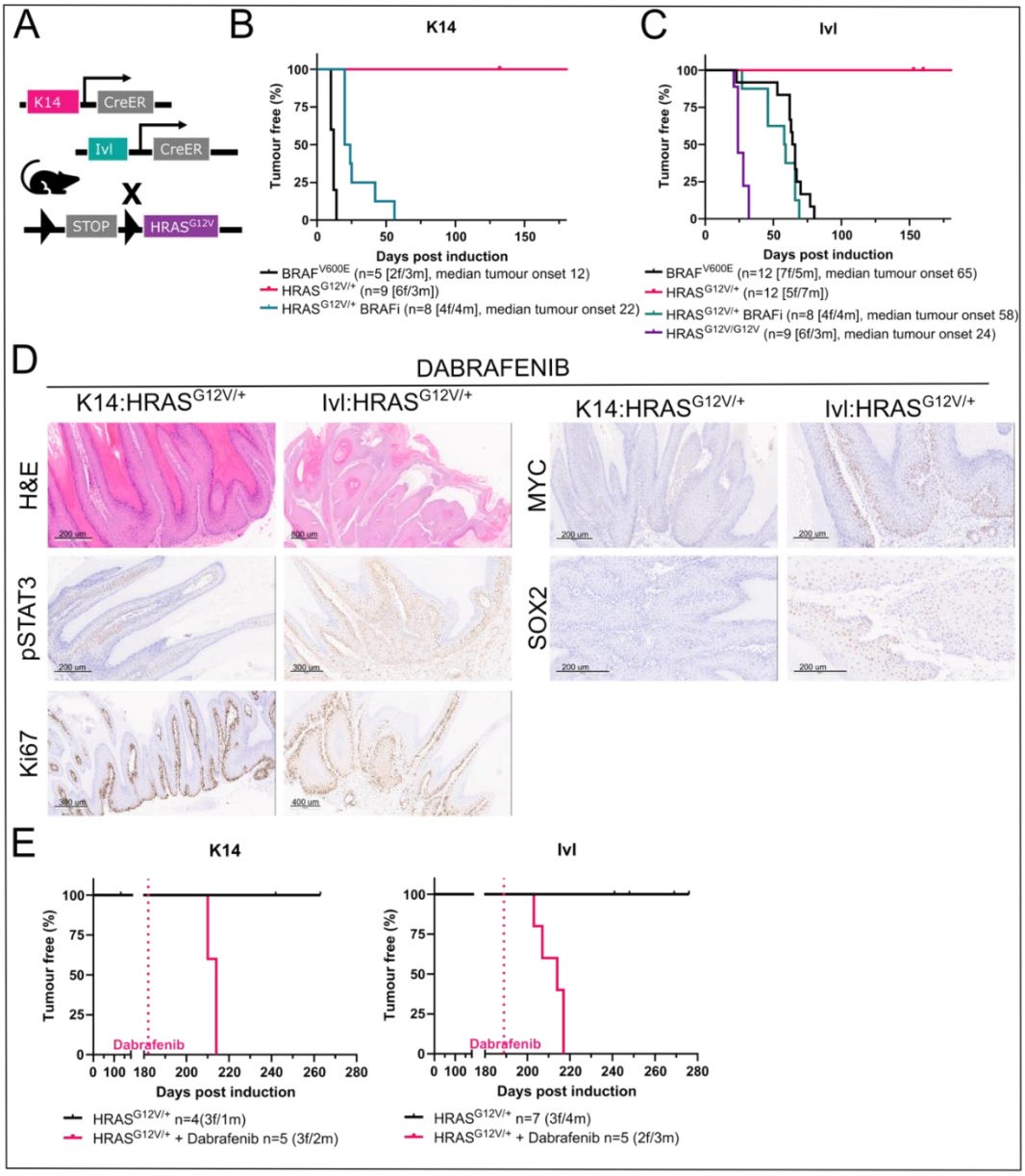

Figure 6. Dabrafenib as a tumour promoter in *HRAS*-mutated epidermis . A, Schematic representation of the mouse models used. **B and C,** Kaplan-Meier tumour-free survival plot for K14:BRAF^{V600E}, K14:HRAS$^{G12V/+}$ and K14:HRAS$^{G12V/+}$ treated with the BRAFi Dabrafenib and TPA (B), and Ivl:BRAF^{V600E}, Ivl:HRAS$^{G12V/+}$, Ivl:HRAS$^{G12V/G12V}$ and K14:HRAS$^{G12V/+}$ treated with BRAFi Dabrafenib (C). Note that K14:BRAF^{V600E} and Ivl:BRAF^{V600E} cohorts correspond to CRUK-SI cohorts shown in Figure 1D and F and are shown here for comparison. **D,** Representative histological images including H&E and IHC of selected markers in tumours derived from K14:HRAS$^{G12V/+}$ and Ivl:HRAS$^{G12V/+}$ mice treated with the BRAFi Dabrafenib at clinical endpoint. **E,** Kaplan-Meier tumour-free survival plots for K14:HRAS$^{G12V/+}$ treated with BRAFi Dabrafenib 182 days after oncogene induction (left) and Ivl:HRAS$^{G12V/+}$ treated with BRAFi Dabrafenib 189 days after oncogene induction (right).